



Alexandria University
Alexandria Engineering Journal

www.elsevier.com/locate/aej
www.sciencedirect.com



ORIGINAL ARTICLE

Revisiting the lid-driven cavity flow problem: Review and new steady state benchmarking results using GPU accelerated code



Tamer A. AbdelMigid^a, Khalid M. Saqr^b, Mohamed A. Kotb^{a,*},
Ahmed A. Aboelfarag^c

^a Department of Marine Engineering, College of Engineering and Technology, Arab Academy for Science, Technology and Maritime Transport, Alexandria, Egypt

^b Department of Mechanical Engineering, College of Engineering and Technology, Arab Academy for Science, Technology and Maritime Transport, Alexandria, Egypt

^c Department of Computer Engineering, College of Engineering and Technology, Arab Academy for Science, Technology and Maritime Transport, Alexandria, Egypt

Received 21 May 2016; revised 10 September 2016; accepted 20 September 2016
Available online 15 October 2016

KEYWORDS

Lid-driven cavity flow;
GPU accelerated;
Numerical method;
CFD;
Finite volume method

Abstract This paper presents a broad account of the lid-driven cavity flow problem which is an important benchmark problem for the validation of CFD codes. A comprehensive review of the literature on the problem is presented and discussed, and available benchmarking results are compared in tabulated format to provide a comprehensive source of validation data. In addition, the problem was solved using a Graphical Processing Unit (GPU) accelerated in-house code developed by the authors (https://github.com/TamerAbdelmigid/DrivenCavity_FVM.git), which solves the steady Navier-Stokes equations, using the Finite Volume Method (FVM) in primitive variable formulation. Case studies of steady incompressible flow in a 2D lid-driven square cavity are investigated for $100 < Re < 5000$. Detailed second order spatially accurate results are verified and presented in a tabulated form for the sake of serving as benchmark dataset for future works on the same problem. In the present work, collocated grid arrangement along with a uniform structured Cartesian grid up to 1301×1301 was used.

© 2016 Faculty of Engineering, Alexandria University. Production and hosting by Elsevier B.V. This is an open access article under the CC BY-NC-ND license (<http://creativecommons.org/licenses/by-nc-nd/4.0/>).

1. Introduction

The driven cavity flow for over the past half a century served as a benchmarking case for anyone to validate their techniques and methods against, and over this period it has been studied by hundreds of authors with nearly every numerical method that exists, and yet only a handful of accurate and complete

* Corresponding author.

E-mail address: kotb2000@yahoo.com (M.A. Kotb).

Peer review under responsibility of Faculty of Engineering, Alexandria University.

<http://dx.doi.org/10.1016/j.aej.2016.09.013>

1110-0168 © 2016 Faculty of Engineering, Alexandria University. Production and hosting by Elsevier B.V.

This is an open access article under the CC BY-NC-ND license (<http://creativecommons.org/licenses/by-nc-nd/4.0/>).

benchmark results are available in the literature. In the present paper, all available data on the problem have been reviewed and discussed in details. In addition, a GPU accelerated finite volume code has been developed and utilized to produce accurate benchmarking results using grids of resolution up to 1301×1301 cells. The purpose of the existing review was to make some of the most important work done on the steady state square driven cavity flow in the past 50 years available in one source. However, it is worth mentioning that the presented review is by no means intended to be comprehensive.

The discussion proposed in the present paper concentrates on the discretization technique, spatial accuracy, grid, and Reynolds number range considered in the literature.

Though all the methods have been used to study the driven cavity case, the Finite Difference method is by far the most used one, from as old as Burggraf [1] to as new as Kalita and Gupta [2]. Most of the authors formulated the governing equations in stream function-vorticity variables, most famous of which are Ghia et al. [3] who used coupled strongly implicit multigrid (CSI-MG) based on the work of Rubin and Khosla [4] method in the solution of the driven flow in a square cavity, for Reynolds number $Re \leq 10,000$. They used a uniform mesh of 257×257 . They presented a Second-order accurate tabulated benchmark results that have served as “The” result to compare against ever since. Recently, Erturk et al. [5] using a fine uniform grid mesh of 601×601 , computed a steady solution for the driven cavity flow for Reynolds number $Re \leq 21,000$ with maximum absolute residuals of the governing equations that were less than 10^{-10} , although their solution was second order spatially accurate, but they provided a six order accurate solution for some variables using Richardson extrapolation.

On the other hand other authors formulated their equations using only the stream function as a variable. Of those we mention Schreiber and Keller [6] who presented fourth-order spatially accurate results for Reynolds number $Re \leq 10,000$. Their numerical methods combined an efficient linear system solver, an adaptive Newton-like method for nonlinear systems, and a continuation procedure for following a branch of solutions over a range of Reynolds numbers, on a 180×180 uniform grid. Also, Pochinapan [7] obtained a solution up to Reynolds number $Re = 5000$ with second-order spatial accuracy on a 122×122 grid.

However, some authors used primitive variables like Vanka [8] who presented a second order accurate solutions for steady flows up to Reynolds Number $Re = 5000$. He used a uniform grid of 321×321 . Bruneau and Saad [9] obtained a steady and periodic solutions for various Reynolds numbers by solving the unsteady Navier-Stokes equations on a 1024×1024 uniform staggered grid. Their numerical simulation lies on a multigrid solver with a cell-by-cell relaxation procedure. Classical Euler or Gear time schemes are coupled to a second-order approximation of the linear terms in space. Convective terms were treated explicitly and approximated by third-order schemes.

Standing apart from them Gupta and Kalita [10], they used stream function-velocity formulation to obtain a second order accurate solution for Reynolds Number $100 \leq Re \leq 10,000$. Their computation was done on uniform 161×161 grid. They used a biconjugate gradient method to obtain the numerical solutions of the aforementioned fluid flow problem.

Second in popularity was the Finite volume method in primitive variable formulation as an example, Wright and Gaskell [11] presented a second and fourth order spatially accurate steady solution for Reynolds number $100 \leq Re \leq 1000$ using the staggered grid arrangement and control volume formulation. They used the Block Implicit Multigrid Method (BIMM) on a very fine uniform mesh of 1024. Similarly, Magalhães et al. [12] presented a second order spatially and temporally accurate solution for Reynolds Number $Re = 100, 400, \text{ and } 1000$ on a non-uniform mesh of 51×51 .

Finite element method takes the third place where Olson and Tuann [13] recasted the full Navier-Stokes equations in the form of a single, fourth order equation for stream function, with an 18 degrees-of-freedom triangular element, such that the velocities were continuous and the incompressibility was satisfied exactly. They covered Reynolds Number from 10^{-4} to $Re = 3450$, with a uniform mesh of 8×8 , and produced a remarkably accurate results for such coarse mesh. Likewise, Barragy and Carey [14] used finite element for the solution of the lid-driven cavity flow up to Reynolds number $Re \leq 12,500$. They used a graded mesh of elements of degree $p = 8$, and they also incorporated an under resolved solution for $Re = 16,000$.

After that comes several other methods such as Lattice Boltzmann which have been used by Hou et al. [15] with compressibility effects, for the solution of the driven cavity flow for Reynolds number $Re \leq 7500$ using a 256×256 grid points. Similarly, Lin et al. [16] used the multi relaxation time (MRT) lattice Boltzmann equation (LBE) with D2Q9 model to compute a steady solution at different Reynolds numbers (100–7500), using a 129×129 grid.

Boundary Element has been used by Grigoriev and Dargush [17] for Reynolds number $Re \leq 5000$. They carried out the simulation on a non-uniform mesh with 1680 hexagonal regions. In addition Aydin and Fenner [18] used it to acquire a solution for low-to-moderate-Reynolds number $0 \leq Re \leq 1200$. They used four different mesh sizes (maximum being 81 Boundary elements).

Smooth particle hydrodynamics has been used by Szwec et al. [19] along with three different incompressibility treatments namely WCSPH, weakly compressible smoothed particle hydrodynamics; ISPH, incompressible smoothed particle hydrodynamics; with two variants PPS, particle-based Poisson solver; GPS, grid-based Poisson solver, to obtain a solution for lid driven cavity at $Re = 1000$, with 57,600 particles. And Khorasanizade and Sousa [20] computed a solution for flow at moderate Reynolds numbers $100 \leq Re \leq 3200$, employing the mesh-free (SPH), with a new treatment for no-slip boundary conditions. They carried out their study using different spatial resolutions maximum of which is $L/200$.

Chebyshev collocation method has been used by Botella and Peyret [21] to present a highly-accurate spectral solutions with extensive benchmark results for the flow at Reynolds number $Re = 1000$ using with a maximum of grid mesh of $N = 160$ (polynomial degree).

Incremental unknowns were utilized by Goyon [22] to solve the unsteady 2D Navier-Stokes equations on an un-regularized driven cavity. They presented steady solution for Reynolds number $Re \leq 7500$. For Reynolds number $10,000 \leq Re \leq 12,500$ they presented a periodic solution, although they admit that this investigation field is less exploited, because of the computational cost.

Differential quadrature (DQ) method was used by Nishida and Satofuka [23] to present higher-order method for the numerical simulation of square driven cavity flows. They discretized the spatial derivatives of the Navier-Stokes equations by means of the modified differential quadrature (MDQ) method. With this they have presented spatially Δh^{10} order accurate solutions with grid size of 129×129 for $Re \leq 3200$.

Fractional step was used by Kim and Moin [24] which is second-order accurate in both space and time. They obtained a numerical solutions for flows inside a driven cavity for Reynolds number $1 \leq Re \leq 5000$ on a mesh of 97×97 .

Discrete singular convolution was utilized by Wan et al. [25] for treating incompressible flows, which they used to obtain an accurate solution for the driven cavity flow problem up to $Re = 10,000$, on a uniform mesh of 201×201 . Their method was third order accurate in time.

Silva and de Moura [26] and Lima et al. [27] used control volume finite element method CVFEM and nine-node elements to study the incompressible, and viscous fluid flow inside a square driven cavity for $Re = 100, 400, 1000$ and $10,000$. Moreover, Ammara and Masson [28] used a fully coupled control-volume finite element method (CVFEM) for solving the two-dimensional incompressible Navier–Stokes equations inside a square cavity for $Re = 400$, and 1000 .

Table 1 summarizes the main feature of each reference mentioned and presents it in a chronological fashion. Discretization scheme utilized is abbreviated in the following manner: (FD) Finite Difference, (FE) Finite Element, (FV) Finite Volume, (MDQ) Modified Differential Quadrature, (LB) Lattice Boltzmann, (IU) Incremental Unknowns, (DSC) Discrete

Singular Convolution, (Cheb.) Chebyshev collocation, (BE) Boundary Element, (SPH) Smooth Particle Hydrodynamic, and (CVFEM) Control Volume Finite Element Method.

It can be seen from the review how important the driven cavity case is. Its importance was stated elegantly and succinctly by Shankar and Deshpande [29] “... internal recirculating flows generated by the motion of one or more of the containing walls. ... are not only technologically important, they are of great scientific interest because they display almost all fluid mechanical phenomena in the simplest of geometrical settings. Thus corner eddies, longitudinal vortices, nonuniqueness, transition, and turbulence all occur naturally and can be studied in the same closed geometry”.

2. Numerical method

The developed code is based on a one developed by Peric 1998 and described by Ferziger and Perić [30]. It was ported from FORTRAN 77 to C++. The code uses Finite Volume Method in primitive variable formulation on a staggered grid. More information on FVM and its advantages can be found in Ferziger and Perić [30] and Versteeg and Malalasekera [31].

Fig. 1 illustrates the program flow chart which can be seen mostly a Semi-Implicit Pressure Linked Equation scheme preceded by a grid generation. The numbered steps represent the SIMPLE scheme and each step composed of both discretization and solution of the resulted linear algebraic equation system. Discretization and interpolation techniques will be explained in details next.

Table 1 The driven cavity flow literature arranged chronologically.

Year	Reference	Disc. scheme	Formulated variables	Spatial $\Delta(O)$	Temp. $\Delta(O)$	Grid	Re
1966	Burggraf [1]	FD	$\psi - \xi$	2	—	40 * 40	0–400
1979	Olson and Tuann [13]	FE	ψ	4	—	8 * 8	0.0001–3450
1982	Ghia et al. [3]	FD	$\psi - \xi$	2	—	257 * 257	100–10,000
1983	Schreiber and Keller [6]	FD	ψ	4	—	180 * 180	1–10,000
1984	Kim and Moin [24]	FS	u, v, p	2	2	97 * 97	1–5000
1985	Vanka [8]	FD	u, v, p	2	—	321 * 321	100–5000
1990	Bruneau and Jouron [32]	FD	u, v, p	2	—	512 * 512	100–15,000
1991	Gupta [33]	FD	$\psi - \xi$	4	—	41 * 41	1–2000
1992	Nishida and Satofuka [23]	MDQ	$\psi - \xi$	10	4	129 * 129	100–3200
1995	Wright and Gaskell [11]	FV	u, v, p	4	—	1024 * 1024	100–1000
1995	Hou et al. [15]	LB	BGK model	—	—	256 * 256	100–7500
1996	Goyon [22]	IU	$\psi - \xi$	2	2	257 * 257	100–7500
1997	Barragy and Carey [14]	FE	$\psi - \xi$	$P = 8$	—	31 * 31	1000–10,000
1998	Botella and Peyret [21]	Cheb.	u, v, p	$N = 160$	—	$N = 160$	1000
1999	Grigoriev and Dargush [17]	BE	u, v, p	—	—	1680 Hex	1000–5000
2001	Aydin and Fenner [18]	BE	u, v, p	—	—	81	0–1200
2001	Silva and de Moura [26]	CVFEM	u, v, p	—	—	30 * 30	100–10,000
2002	Wan et al. [25]	DSC	u, v, p	—	3	201 * 201	1000–10,000
2004	Lima et al. [27]	CVFEM	u, v, p	—	—	161 * 161	100–10,000
2004	Ammara and Masson [28]	CVFEM	u, v, p	—	—	128 * 128	400–1000
2005	Gupta and Kalita [10]	FD	$\psi - u, v$	2	—	161 * 161	100–10,000
2010	Kalita and Gupta [2]	FD	$\psi - \xi$	2	2	161 * 161	1000–10,000
2011	Lin et al. [16]	LB	D2Q9 model	—	—	129 * 129	100–7500
2012	Szewc et al. [19]	SPH	u, v, p	—	—	57,600	1000
2012	Poohinapan [7]	FD	ψ	2	—	122 * 122	100–5000
2013	Magalhães et al. [12]	FV	u, v, p	2	2	6910	1000
2014	Khorasanizade and Sousa [20]	SPH	u, v, p	—	—	$L/200$	100–3200

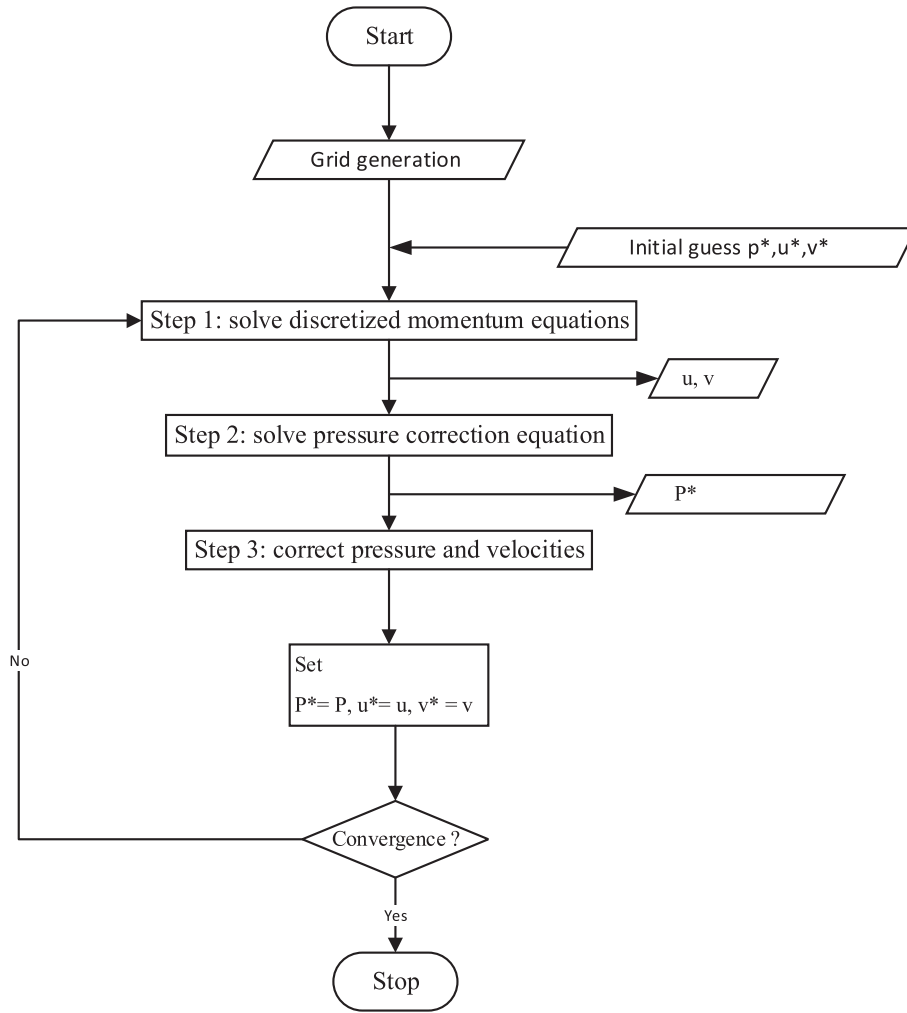


Figure 1 Ported code flowchart.

Next, discretization and interpolation techniques will be explained in details, and we start by presenting an implicit finite volume scheme that uses the pressure-correction method on a staggered two-dimensional Cartesian grid.

The Navier-Stokes equations in integral form reads:

$$\int_S \rho \mathbf{v} \cdot \mathbf{n} dS = 0 \quad (2.1)$$

$$\begin{aligned} \int_{\Omega} \rho u_i d\Omega + \int_S \rho u_i \mathbf{v} \cdot \mathbf{n} dS &= \int_S \tau_{ij} i_j \cdot \mathbf{n} dS - \int_S p i_i \cdot \mathbf{n} dS \\ &+ \int_{\Omega} (\rho - \rho_0) g_i d\Omega \end{aligned} \quad (2.2)$$

The macroscopic momentum flux vector τ_i , is split into a viscous contribution $\tau_{ij} i_j$ and a pressure contribution $p i_i$. We assume the density constant. The mean gravitational force is incorporated into the pressure term. Typical staggered control volume which are shown in Fig. 2 was used, where the control volumes for u_x and u_y are displaced with respect to the control volume for the continuity equation. Cell faces 'e' and 'w' for u and 'n' and 's' for v lie midway between the nodes.

We now consider the approximation of the convective, diffusive fluxes and the source terms. The surface integrals may be split into four CV face integrals. The second order central difference approximations were adopted. Fluxes are approximated by assuming that the value of a quantity at a CV face center represents the mean value over the face (midpoint rule approximation). On the m th outer iteration, all nonlinear terms are approximated by a product of an 'old' (from the preceding outer iteration) and a 'new' value. Thus, in discretizing the momentum equations, the mass flux through each CV face is evaluated using the existing velocity field and is assumed known.

For the pressure-velocity decoupling SIMPLE algorithm was used, where the linearized momentum equations are solved with the sequential solution method, using the 'old' mass fluxes and the pressure from the previous outer iteration.

As for the boundary condition, at walls the no-slip boundary condition applies, i.e. the velocity of the fluid is equal to the wall velocity, a Dirichlet boundary condition. However, there is another condition that can be directly imposed in a FV method; the normal viscous stress is zero at a wall. This follows from the continuity equation, e.g. for a wall at $y = 0$.

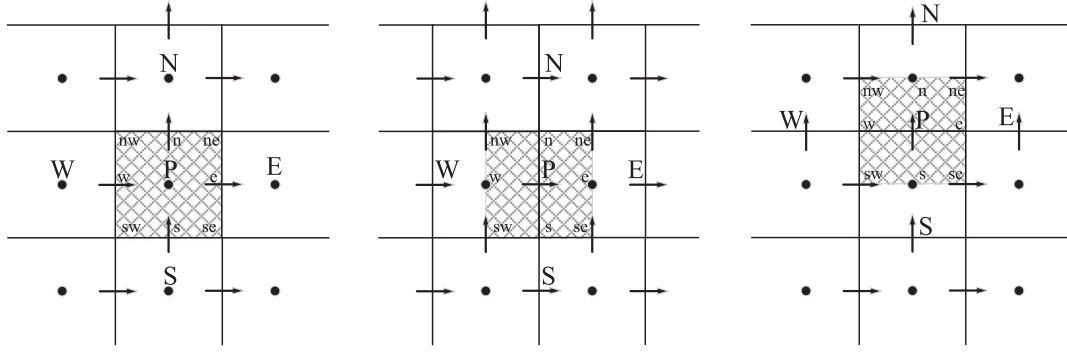


Figure 2 Control volumes for a staggered grid: for mass conservation and scalar quantities (left), for x -momentum (center) and for y -momentum (right).

$$\left(\frac{\delta u}{\delta x}\right)_{wall} = 0 \Rightarrow \left(\frac{\delta v}{\delta y}\right)_{wall} = 0 \Rightarrow \tau_{yy} = 2\mu \left(\frac{\delta v}{\delta y}\right)_{wall} = 0 \quad (2.3)$$

Therefore, the diffusive flux in the v equation at the south boundary is as follows:

$$F_s^d = \int_{S_s} \tau_{yy} ds = 0 \quad (2.4)$$

This was done directly, rather than using only the condition that $v = 0$ at the wall. Since $u_p \neq 0$, we would obtain a non-zero derivative in the discretized flux expression if this was not done; $v = 0$ is used as a boundary condition in the continuity equation. The shear stress can be calculated by using a one-sided approximation of the derivative $\delta u / \delta y$; one possible approximation is as follows:

$$F_s^d = \int_{S_s} \tau_{xy} ds = \int_{S_s} \mu \frac{\delta u}{\delta y} ds \approx \mu_s S_s \frac{u_p - u_s}{y_p - y_s} \quad (2.5)$$

In a FV method using a staggered grid, the pressure is not required at boundaries. This is due to the fact that the nearest CV for the velocity component normal to the boundary extends only up to the center of the scalar CV, where the pressure is calculated.

When the approximations for all the fluxes and source terms are substituted into Eqs. (2.1) and (2.2), we obtain a set of algebraic equations, which we can put in the form:

$$Ax = b. \quad (2.6)$$

Now, for the solution of the resulted system of linear equations, the strongly implicit procedure (SIP) Stone [34] was used, and a brief explanation of the steps will be presented. First the matrix A is decomposed in the following way:

$$A \approx LU = M = A + N. \quad (2.7)$$

L and U are a lower and upper triangle matrix. A multiplication of L and U yields diagonals which are not part of matrix A . These are put in N . N can be considered as some sort of error of the decomposition. To minimize the deviation it is required

$$(A + n)x \approx b \Rightarrow Nx \approx 0. \quad (2.8)$$

That the coefficients on these extra diagonals were to be approximated by their neighbor coefficients. A linear approximation with a parameter α can be made to determine these coefficients. That is

$$x_{NW} \approx \alpha(x_W + x_N - x_P) \quad (2.9)$$

It is now possible to receive a set of implicit rules for the calculation of the coefficients of L and U . At step n we have

$$Ax^n = b - r^n \quad (2.10)$$

with r^n as the residual. The deviation of x^n from the real solution x is called convergence error ϵ^n

$$\epsilon^n = x - x^n \quad (2.11)$$

Therefore one yields

$$A\epsilon^n = Ax - Ax^n = b - b + r^n = r^n \Rightarrow A\epsilon^n = r^n \quad (2.12)$$

As the real x is unknown, we construct an iterative rule:

$$\begin{aligned} A(x^{n+1} - x^n) &= r^n \\ A\Delta x &= LU\Delta x = r^n \\ U\Delta x &= L^{-1}r^n = R^n \end{aligned} \quad (2.13)$$

Having done the decomposition we are now able to calculate the residual r^n , the vector R^n and finally Δx . The algorithm can now be formulated as can be seen in Fig. 3.

In step 2 of the algorithm L^{-1} will not be calculated directly. Instead, an implicit rule will be used, and hence the method is named strongly implicit, Reeve et al. [35].

We used a 1D-array (index l) to store the nodes in order to get optimal memory access. Therefore, a mapping from 2D- to 1D-coordinates was necessary. A parallel version of stone's strongly implicit procedure presented in Reeve et al. [35] was used. Fig. 4 shows the modified iteration space dependence graph after the nested loops have been skewed using wavefront method, Wolfe [36], which enable parallel implementation of the SIP solver.

Two platforms were used throughout the work, platform 1 "CPU: Intel i7 5820 K @3.6 GHz – 6C/12T || GPU: NVIDIA GTX TITAN @876 MHz – 2688 cores" and platform 2 "CPU: Intel i7 4710HQ @2.6 GHz – 4C/8T || GPU: NVIDIA GTX 860 M @1029 MHz – 680 cores" From now on, reference will be made to the used platforms by platform 1 or platform 2.

3. GPU implementation of SIP

In this section two implementations namely kernels will be discussed, and for clarity sake only forward substitution step will be mentioned in detail. The same concepts are applied to backward substitution step. All tests were run using grid

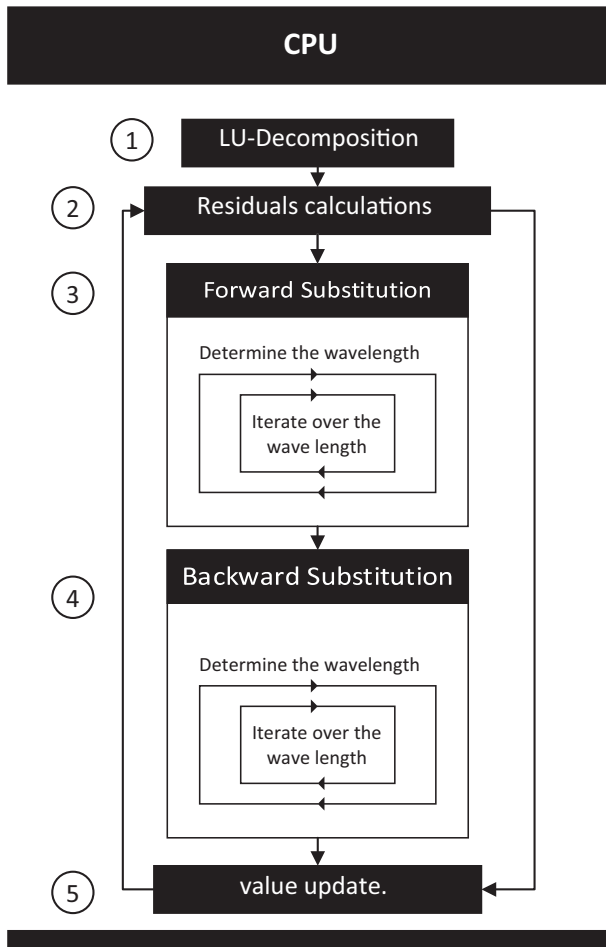


Figure 3 SIP algorithm.

dimensions ranging from 1001^2 to 6001^2 a range that is limited by available memory in the used testing platform “platform 2”. Only steps 3 and 4 are moved to the GPU for acceleration as step 2 involves a variable update each iteration which would

require a reduction algorithm if it was to be moved to the GPU, as there is no instruction to provide such a function directly in CUDA C as opposed to OpenMP, Dagum and Menon [37].

3.1. Kernel 1 “Optimized Blocks of Threads”

With the first implementation LU decomposition step is done on the CPU after that the necessary matrices are allocated and transferred to GPU global memory. After that, an outer loop that involves steps 2–5 is entered where the exit conditions are either preset residuals or a preset loop counter is reached. Inside that loop the residual calculation step is done on the CPU and then the RES matrix is transferred to GPU as can be seen in Fig. 5.

Then, the inner loop of the Forward substitution step is executed on the GPU. It is of great importance to know that compute resource partitioning requires special attention in CUDA programming. The computer resources limit the number of active warps. Therefore, one must be aware of the restrictions imposed by the hardware, and the resources used by one’s kernel. In order to maximize GPU utilization, it is required to maximize the number of active warps.

Table 2 presents the threads per block per iteration execution time for grid dimension of 6001^2 . It can be seen that 64 threads per block give the best performance. For that the blocks were chosen to consist of 2 warps which means each block will contain 64 threads and the number of blocks will be determined based on the currently executed wavelength.

Manipulating thread blocks to either extreme can restrict resource utilization, Cheng et al. [38]:

- Small thread blocks: Too few threads per block lead to hardware limits on the number of warps per SM to be reached before all resources are fully utilized.
- Large thread blocks: Too many threads per block lead to fewer per-SM hardware resources available to each thread.

As it can be seen in Fig. 6 Kernel 1 is slower than the parallel CPU implementation in grid sizes less than 4000^2 where

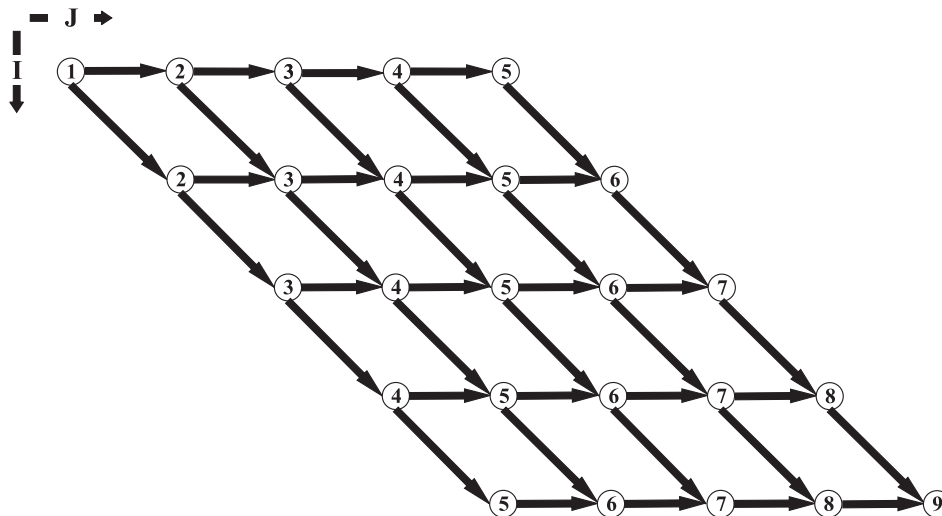


Figure 4 Modified iteration space dependence graph after loop skewing.

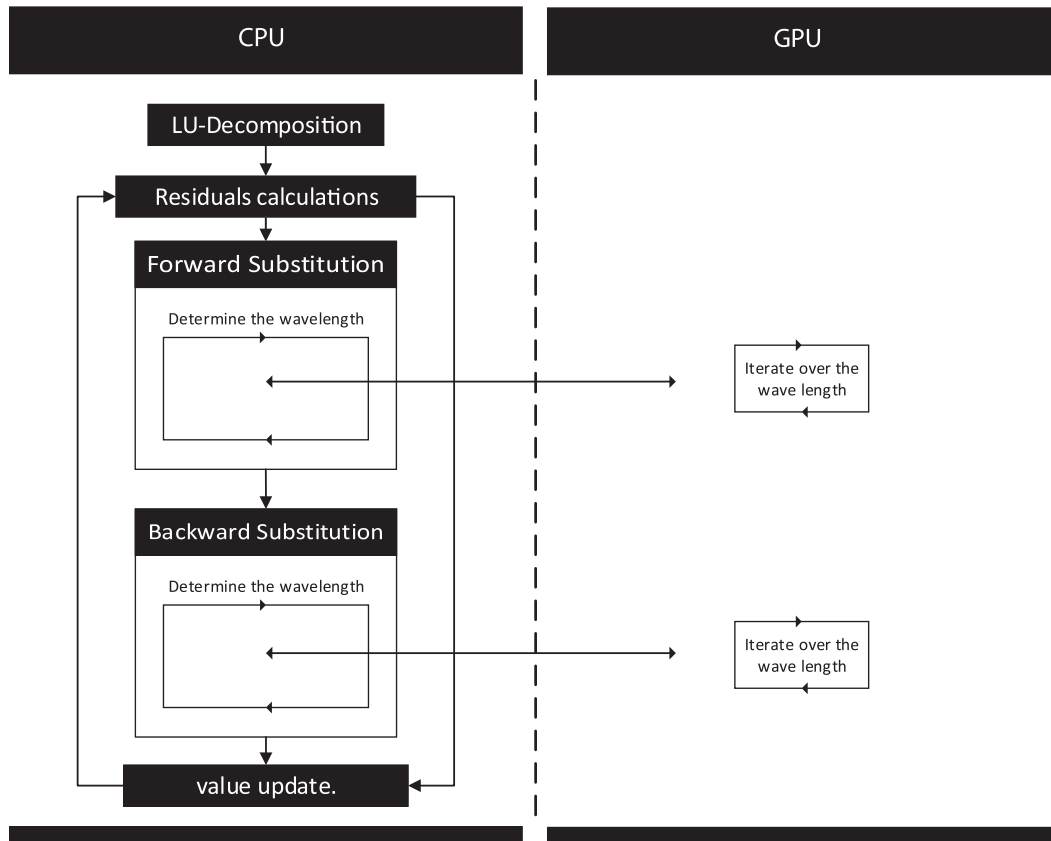


Figure 5 Kernel 1 “Optimized Blocks of Threads”.

Table 2 Threads per block execution time in seconds.

Threads per block	Time in sec
32	41.8
64	41
128	42.5
256	43.9
512	42.6
1024	44.3

the initialization and data transfer to GPU memory overhead exceed the acceleration in execution offered by the GPU. It is also evident that Kernel 2 offers an increased acceleration over Kernel 1 implementation due to the elimination of the initialization overhead and reduced memory transfer. Yet, as the grid size increases the problem becomes more dependent on memory and hence the drop in acceleration noticed in Fig. 6. So, still some work needs to be done to optimize memory transfer and in order to prevent the memory dependence enabling further acceleration.

3.2. Kernel 2 “Dynamic Parallelism”

By implementing dynamic parallelism kernel launching from CPU overhead can be greatly reduced which in turn would improve the performance. Using this concept the program was adjusted as follows as can be seen in Fig. 7, where the

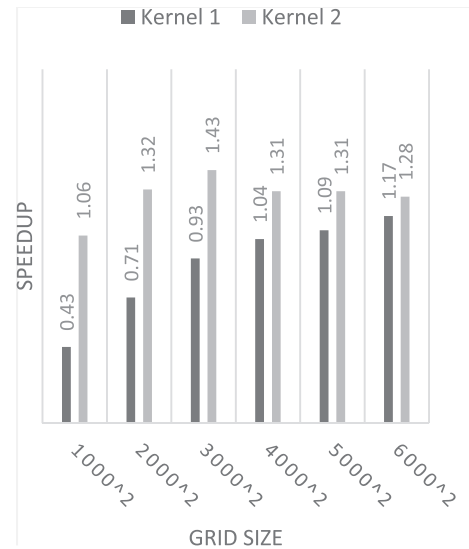


Figure 6 Speedup of Kernel 1 and 2 over parallel CPU implementation of SIP algorithm.

forward substitution parent kernel is launched from the host, and it encloses a call to forward substitution child kernel mentioned previously which will be launched repeatedly from the device.

By implementing the dynamic parallelism, the solution time was managed to be reduced by 30% compared to the parallel implementation on the CPU which is translated to a 1.43 X speedup as can be seen in Fig. 6.

4. Result and discussion

Fig. 8 illustrates the configuration utilized in solving the driven cavity case, where at top wall “the lid” moves in the positive x direction with unit velocity, and the velocity at the remaining three walls equals zero. The range of Reynolds Numbers considered $100 \leq Re \leq 5000$ which according to [39–44] these Reynolds numbers $Re \leq 5000$ are well in the steady state range. The Reynolds number was controlled using various values for the dynamic viscosity μ . Solution is believed to be converged when maximum RMS of the residuals is less than or equal to 10^{-8} .

For each case a three consecutive refined meshes were used to obtain the solution in order to use Richardson extrapolation on some of the key results to obtain a more accurate solution up to Δh^6 . A uniform mesh of 601×601 is used for Reynolds number $Re \leq 3200$. For Reynolds number $Re = 5000$ it was difficult to obtain steady solution on such a mesh so the mesh was refined further to reach 1301×1301 , although a converged solution was obtained on 801×801 , but we choose to display the results from the former. Also, as mentioned a three consecutive refined mesh is needed for Richardson extrapolation.

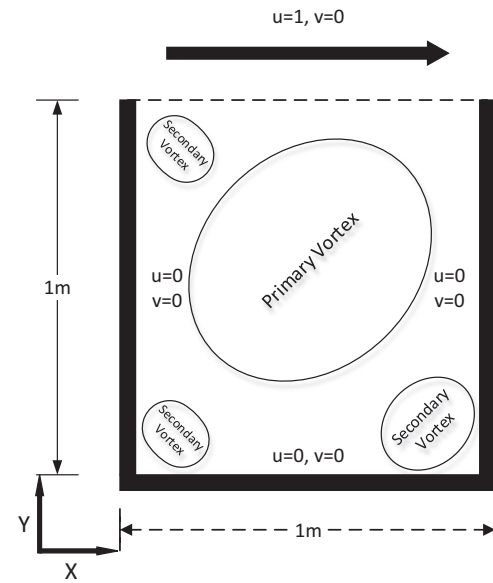


Figure 8 Schematic diagram of the lid-driven cavity case.

4.1. Vortices main properties

Tables 3–7 contain primary, secondary, and tertiary vortices main properties (Stream function, vorticity, and location),

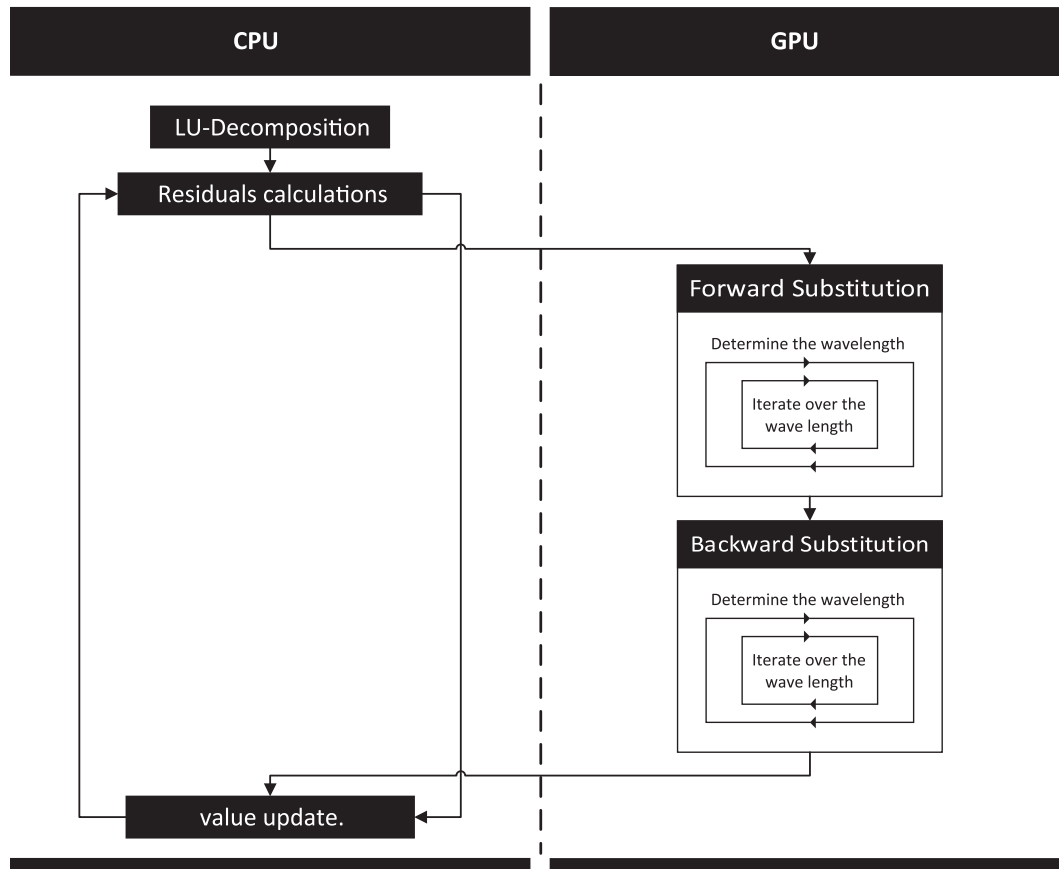


Figure 7 Kernel 2 “Dynamic Parallelism”.

Table 3 Primary and secondary vortices main properties at $Re = 100$.

Reynolds number		100				
Reference		Present	Ghia	Schriber	Vanka	Wright
Primary vortex	Ψ	-0.103516	-0.103423	-0.1033	0.1034	0.103516
	ω	3.156202	3.16646	-3.182	-	3.17044
	(x, y)	0.6156, 0.7371	0.6172, 0.7344	0.6167, 0.7417	0.6188, 0.7375	0.6157, 0.7378
BR1	Ψ	0.000013	1.25374E-05	0.0000132	-0.0000114	-1.25374E-05
	ω	-0.035775	-0.0330749	0.0255	-	-0.0330749
	(x, y)	0.9418, 0.0616	0.9453, 0.0625	0.9417, 0.05	0.9375, 0.0563	0.9453, 0.0625
BL1	Ψ	1.80683E-06	1.74877E-06	0.00000205	-0.00000194	-1.79705E-06
	ω	-0.01340214	-0.0155509	0.00798	-	-0.0146139
	(x, y)	0.0333, 0.0349	0.0313, 0.0391	0.0333, 0.025	0.0375, 0.0313	0.0337, 0.0347

Table 4 Primary and secondary vortices main properties at $Re = 400$.

Reynolds number		400				
Reference		Present	Ghia	Schriber	Vanka	Shuling Hou
Primary vortex	Ψ	-0.113964	-0.113909	-0.11297	0.1136	0.1121
	ω	2.295985	2.29469	2.281	-	-
	(x, y)	0.5541, 0.6057	0.5547, 0.6055	0.5571, 0.6071	0.5563, 0.6	0.5608, 0.6078
BR1	Ψ	0.000645	0.000642352	0.000644	-0.000645	-0.000619
	ω	-0.44839	-0.433519	0.394	-	-
	(x, y)	0.8852, 0.1215	0.8906, 0.1250	0.8857, 0.1143	0.8875, 0.1188	0.8902, 0.1255
BR2	Ψ	-1.94847E-08	-1.86595E-08	-	-	-
	ω	0.003591006	0.00438726	-	-	-
	(x, y)	0.9917, 0.0067	0.9922, 0.0078	-	-	-
BL1	Ψ	1.43588E-05	1.41951E-05	0.0000145	-0.00146	0.000013
	ω	0.05471926	0.0569697	0.0471	-	-
	(x, y)	0.0516, 0.0466	0.0508, 0.0469	0.05, 0.0429	0.05, 0.05	0.0549, 0.0510

Table 5 Primary and secondary vortices main properties at $Re = 1000$.

Reynolds number		1000				
Reference		Present	Ghia	Schriber	Botella	Erturk
Primary vortex	Ψ	-0.118866	-0.117929	-0.11603	0.1189366	-0.118781
	ω	2.066581	2.04968	-2.026	2.067753	-2.06553
	(x, y)	0.5308, 0.5657	0.5313, 0.5625	0.5286, 0.5643	0.5308, 0.5625	0.53, 0.565
BR1	Ψ	0.001732	0.00175102	0.0017	-0.00175102	0.0017281
	ω	-1.113969	-1.15465	0.999	-1.15465	1.115505
	(x, y)	0.8636, 0.1115	0.8594, 0.1094	0.8643, 0.1071	0.8594, 0.1094	0.8633, 0.1117
BR2	Ψ	-5.46775E-08	-9.31929E-08	-	5.03944E-08	-5.4962E-08
	ω	0.006969814	0.00852782	-	-	-0.0077076
	(x, y)	0.9917, 0.0067	0.9922, 0.0078	-	0.9923, 0.0077	0.9917, 0.0067
BL1	Ψ	0.000233412	0.000231129	0.000217	-0.000233453	0.00023261
	ω	-0.3409262	-0.36175	0.302	-0.3522861	0.353473
	(x, y)	0.0832, 0.0782	0.0859, 0.0781	0.0857, 0.0714	0.0833, 0.0781	0.0833, 0.0783

Table 6 Primary and secondary vortices main properties at $Re = 3200$.

Reynolds number		3200				
Reference		Present	Ghia	Goyon	Grigoriev	Nishida
Primary vortex	Ψ	-0.121566	-0.120377	-0.1122	-0.1218	-0.121154
	ω	1.957201	1.9886	—	—	-1.950781
	(x, y)	0.5175, 0.5408	0.5165, 0.5469	0.5234, 0.5468	0.518, 0.540	0.5156, 0.5391
BR1	Ψ	0.002837	0.00313955	0.00262	0.00288	0.00281924
	ω	-2.234296	-2.27365	—	—	2.10559
	(x, y)	0.8236, 0.0849	0.8125, 0.0859	0.8281, 0.0859	0.824, 0.085	0.8281, 0.0859
BR2	Ψ	-2.07365E-07	-2.51648E-07	0.00000015	—	1.59854E-07
	ω	0.01371044	0.0097423	—	—	-0.0153772
	(x, y)	0.9884, 0.0099	0.9844, 0.0078	0.9844, 0.0078	—	0.9922, 0.0078
BL1	Ψ	0.001113952	0.00097823	0.000993	0.00113	0.00110595
	ω	-1.137424	-1.06301	—	—	1.22436
	(x, y)	0.08153, 0.1198	0.0859, 0.1094	0.0859, 0.1171	0.082, 0.119	0.0781, 0.125
TL1	Ψ	0.000710328	0.000727682	0.000638	0.000721	0.000745436
	ω	-1.69611	-1.71161	—	—	1.58028
	(x, y)	0.0533, 0.9002	0.0547, 0.8984	0.0546, 0.9062	0.054, 0.897	0.0547, 0.8984

Table 7 Primary and secondary vortices main properties at $Re = 5000$.

Reynolds number		5000				
Reference		Present	Ghia	Erturk	Burnea 1990	Gupta
Primary vortex	Ψ	-0.122069	-0.118966	-0.121289	-0.1142	-0.122
	ω	-1.938057	1.86016	-1.926601	—	—
	(x, y)	0.5155, 0.5355	0.5117, 0.5352	0.515, 0.535	0.5156, 0.5313	0.5125, 0.5375
BR1	Ψ	0.003078	0.00308358	0.0030604	0.00465	0.00296
	ω	-2.750446	-2.66354	2.274481	—	—
	(x, y)	0.8052, 0.07293	0.8086, 0.0742	0.805, 0.0733	0.8301, 0.0703	0.8, 0.075
BR2	Ψ	-1.45098E-06	-1.43226E-06	-0.000001401	-0.0000247	-0.0000017
	ω	0.03590488	0.0319311	-0.034108	—	—
	(x, y)	0.9780, 0.0189	0.9805, 0.0195	0.9783, 0.0183	0.9668, 0.0293	0.975, 0.0188
BL1	Ψ	0.001375483	0.00136119	0.001517	0.00222	-0.00132
	ω	-1.494181	-1.53055	1.838156	—	—
	(x, y)	0.0729, 0.1369	0.0703, 0.1367	0.79, 0.065	0.0664, 0.1484	0.075, 0.1313
TL1	Ψ	0.001447732	0.00145641	0.0021119	0.00175	0.00154
	ω	-2.065072	-2.08843	2.201598	—	—
	(x, y)	0.0639, 0.9091	0.0625, 0.9102	0.0667, 0.9133	0.0625, 0.9102	0.0688, 0.9125

each of which is compared to four results found in the literature. Vortices are coded with two letters and a number, the first letter indicates either bottom (B) or top (T), while the second letter indicates right (R) or left (L); finally, the number indicates either its secondary (1) or tertiary (2). Ex. BR1 = Secondary Bottom Right.

In each table the present study results are presented along with four of which is believed to be the most accurate results found in the literature, for the sake of comparison.

It can be seen from Table 3 the absence of top left vortices at $Re = 100$, and the presence of only secondary vortices can be detected. At $Re = 400$, the first tertiary vortex is noticeable

at the bottom right corner. As can be seen from Table 4 only Ghia et al. [3] were able to observe and present it, and our results are in good agreement with theirs.

For $Re = 1000$, it's apparent that there was an excellent agreement of our results with those found in the literature. As indicated in Table 6 at $Re = 3200$ the top left vortex starts to appear.

4.2. Velocities

Tables 8 and 9 contain a u , and v -velocity along a vertical and horizontal lines passing through the geometrical center of the

Table 8 Tabulated u -velocity profiles along a vertical line passing through the geometric center of the cavity at various Reynolds numbers.

Point	Y	RE = 100	RE = 400	RE = 1000	RE = 3200	RE = 5000
1302	1.0000	1.0000	1.0000	1.0000	1.0000	1.0000
1272	0.9766	0.8500	0.7698	0.6756	0.5360	0.5015
1262	0.9688	0.8057	0.7061	0.6009	0.4886	0.4782
1252	0.9609	0.7512	0.6333	0.5284	0.4661	0.4771
1241	0.9531	0.6982	0.5695	0.4776	0.4610	0.4780
1109	0.8516	0.2398	0.2931	0.3383	0.3491	0.3494
957	0.7344	0.0070	0.1648	0.1908	0.2035	0.2047
804	0.6172	-0.1379	0.0221	0.0580	0.0780	0.0818
651	0.5000	-0.2091	-0.1150	-0.0620	-0.0369	-0.0321
590	0.4531	-0.2140	-0.1711	-0.1079	-0.0808	-0.0752
367	0.2813	-0.1580	-0.3286	-0.2794	-0.2414	-0.2359
224	0.1719	-0.1019	-0.2441	-0.3883	-0.3445	-0.3375
133	0.1016	-0.0648	-0.1472	-0.3018	-0.4314	-0.4169
92	0.0703	-0.0469	-0.1038	-0.2238	-0.4081	-0.4456
82	0.0625	-0.0419	-0.0947	-0.2019	-0.3839	-0.4360
72	0.0547	-0.0368	-0.0809	-0.1794	-0.3530	-0.4153
0	0.0000	0.0000	0.0000	0.0000	0.0000	0.0000

Table 9 Tabulated v -velocity profiles along a horizontal line passing through the geometric center of the cavity at various Reynolds numbers.

Point	X	RE = 100	RE = 400	RE = 1000	RE = 3200	RE = 5000
1302	1.0000	1.0000	1.0000	1.0000	1.0000	1.0000
1262	0.9688	-0.0580	-0.1157	-0.2103	-0.4106	-0.5121
1252	0.9609	-0.0747	-0.1538	-0.2798	-0.5049	-0.5689
1241	0.9531	-0.0911	-0.1928	-0.3464	-0.5560	-0.5726
1231	0.9453	-0.1041	-0.2240	-0.3948	-0.5671	-0.5460
1181	0.9063	-0.1750	-0.3855	-0.5265	-0.4462	-0.4314
1119	0.8594	-0.2323	-0.4539	-0.4306	-0.3799	-0.3776
1048	0.8047	-0.2536	-0.3883	-0.3221	-0.3148	-0.3112
651	0.5000	0.0575	0.0521	0.0258	0.0142	0.0117
306	0.2344	0.1796	0.3033	0.3240	0.2864	0.2809
296	0.2266	0.1794	0.3037	0.3333	0.2954	0.2883
204	0.1563	0.1652	0.2840	0.3767	0.3753	0.3649
123	0.0938	0.1266	0.2319	0.3330	0.4318	0.4407
102	0.0781	0.1127	0.2123	0.3112	0.4224	0.4468
92	0.0703	0.1040	0.1994	0.2968	0.4109	0.4433
82	0.0625	0.0947	0.1849	0.2802	0.3949	0.4336
0	0.0000	0.0000	0.0000	0.0000	0.0000	0.0000

cavity, taken at the same location as Ghia et al. [3], and several others for ease of comparison.

4.3. Extrapolated values

Table 10 presents the extrapolated values for primary eddy strength for various Reynolds numbers up to $O(\Delta h_6)$, and it is worth noticing how close our second order accurate results are from the extrapolated six order results, which account for near grid dependence is achieved and that's why the change is nearly negligible.

5. Conclusion

Numerical solution of the 2D incompressible steady Navier-stokes equations is obtained for lid-driven square cavity case for Reynolds Numbers $100 < Re < 5000$, using Finite Volume Method with primitive variable formulation on a uniform grid. Convective terms are discretized using second order central differencing scheme, and SIMPLE algorithm is used to decouple velocity and pressure. Strongly Implicit Procedure was used to solve the resulted linear algebraic equations. Results are presented in tabulated form and agree well with

Table 10 Richardson's extrapolated values for main eddy strength up to six order for various Reynolds numbers.

RE	Grid	$\Psi O(\Delta h^2)$	$\Psi O(\Delta h^4)$	$\Psi O(\Delta h^6)$
100	401	0.1035100		
	501	0.1035130	0.1035183	
	601	0.1035160	0.1035228	0.1035330
400	401	0.1139330		
	501	0.1139530	0.1139887	
	601	0.1139640	0.1139836	0.1139721
1000	401	0.1187800		
	501	0.1188360	0.1189358	
	601	0.1188660	0.1189195	0.1188822
3200	401	0.1212600		
	501	0.1214570	0.1218082	
	601	0.1215660	0.1217603	0.1216513
5000	801	0.1219920		
	901	0.1220340	0.1221089	
	1001	0.122069	0.1221314	0.12218269

those found in the literature. Tertiary vortices in the bottom right corner were observed and reported, and their values are in good agreement with those found in the literature. Velocity profiles agree well with Burggraf [1] prediction.

References

- [1] O.R. Burggraf, Analytical and numerical studies of the structure of steady separated flows, *J. Fluid Mech.* 24 (1966) 113–151.
- [2] J.C. Kalita, M.M. Gupta, A streamfunction–velocity approach for 2D transient incompressible viscous flows, *Int. J. Numer. Meth. Fluids* 62 (2010) 237–266.
- [3] U. Ghia, K.N. Ghia, C. Shin, High- Re solutions for incompressible flow using the Navier-Stokes equations and a multigrid method, *J. Comput. Phys.* 48 (1982) 387–411.
- [4] S. Rubin, P. Khosla, Polynomial interpolation methods for viscous flow calculations, *J. Comput. Phys.* 24 (1977) 217–244.
- [5] E. Erturk, T.C. Corke, C. Gökçöl, Numerical solutions of 2-D steady incompressible driven cavity flow at high Reynolds numbers, *Int. J. Numer. Meth. Fluids* 48 (2005) 747–774.
- [6] R. Schreiber, H. Keller, Driven cavity flows by efficient numerical techniques, *J. Comput. Phys.* 49 (1983) 310–333.
- [7] K. Poochinapan, Numerical implementations for 2D lid-driven cavity flow in stream function formulation, *ISRN Appl. Math.* 2012 (2012).
- [8] S.P. Vanka, Block-implicit multigrid solution of Navier-Stokes equations in primitive variables, *J. Comput. Phys.* 65 (1986) 138–158.
- [9] C.-H. Bruneau, M. Saad, The 2D lid-driven cavity problem revisited, *Comput. Fluids* 35 (2006) 326–348.
- [10] M.M. Gupta, J.C. Kalita, A new paradigm for solving Navier-Stokes equations: streamfunction–velocity formulation, *J. Comput. Phys.* 207 (2005) 52–68.
- [11] N. Wright, P. Gaskell, An efficient multigrid approach to solving highly recirculating flows, *Comput. Fluids* 24 (1995) 63–79.
- [12] J.P. Magalhães, D.M. Albuquerque, J.M. Pereira, J.C. Pereira, Adaptive mesh finite-volume calculation of 2D lid-cavity corner vortices, *J. Comput. Phys.* 243 (2013) 365–381.
- [13] M.D. Olson, S.-Y. Tuann, New finite element results for the square cavity, *Comput. Fluids* 7 (1979) 123–135.
- [14] E. Barragy, G. Carey, Stream function-vorticity driven cavity solution using p finite elements, *Comput. Fluids* 26 (1997) 453–468.
- [15] S. Hou, Q. Zou, S. Chen, G. Doolen, A.C. Cogley, Simulation of cavity flow by the lattice Boltzmann method, *J. Comput. Phys.* 118 (1995) 329–347.
- [16] L.-S. Lin, Y.-C. Chen, C.-A. Lin, Multi relaxation time lattice Boltzmann simulations of deep lid driven cavity flows at different aspect ratios, *Comput. Fluids* 45 (2011) 233–240.
- [17] M. Grigoriev, G. Dargush, A poly-region boundary element method for incompressible viscous fluid flows, *Int. J. Numer. Meth. Eng.* 46 (1999) 1127–1158.
- [18] M. Aydin, R.T. Fenner, Boundary element analysis of driven cavity flow for low and moderate Reynolds numbers, *Int. J. Numer. Meth. Fluids* 37 (2001) 45–64.
- [19] K. Szewc, J. Pozorski, J.P. Minier, Analysis of the incompressibility constraint in the smoothed particle hydrodynamics method, *Int. J. Numer. Meth. Eng.* 92 (2012) 343–369.
- [20] S. Khorasanizade, J.M. Sousa, A detailed study of lid-driven cavity flow at moderate Reynolds numbers using Incompressible SPH, *Int. J. Numer. Meth. Fluids* 76 (2014) 653–668.
- [21] O. Botella, R. Peyret, Benchmark spectral results on the lid-driven cavity flow, *Comput. Fluids* 27 (1998) 421–433.
- [22] O. Goyon, High-Reynolds number solutions of Navier-Stokes equations using incremental unknowns, *Comput. Methods Appl. Mech. Eng.* 130 (1996) 319–335.
- [23] H. Nishida, N. Satofuka, Higher-order solutions of square driven cavity flow using a variable-order multi-grid method, *Int. J. Numer. Meth. Eng.* 34 (1992) 637–653.
- [24] J. Kim, P. Moin, Application of a fractional-step method to incompressible Navier-Stokes equations, *J. Comput. Phys.* 59 (1985) 308–323.
- [25] D. Wan, Y. Zhou, G. Wei, Numerical solution of incompressible flows by discrete singular convolution, *Int. J. Numer. Meth. Fluids* 38 (2002) 789–810.
- [26] J.B.C. Silva, L.F.M. de Moura, A control-volume finite-element method (CVFEM) for unsteady, incompressible, viscous fluid flows, *Numer. Heat Transfer: B Fundam.* 40 (2001) 61–82.
- [27] R. Lima, J. Campos-Silva, S. Mansur, Large eddy simulation of turbulent incompressible fluid flows by a nine-nodes control volume-finite element method, in: *Proceedings of the 10th Brazilian Congress of Thermal Sciences and Engineering–ENCIT 2004*, 2004.
- [28] I. Ammara, C. Masson, Development of a fully coupled control-volume finite element method for the incompressible Navier-Stokes equations, *Int. J. Numer. Meth. Fluids* 44 (2004) 621–644.

- [29] P. Shankar, M. Deshpande, Fluid mechanics in the driven cavity, *Annu. Rev. Fluid Mech.* 32 (2000) 93–136.
- [30] J.H. Ferziger, M. Perić, *Computational Methods for Fluid Dynamics*, third, rev. ed., Springer, Berlin; New York, 2002.
- [31] H.K. Versteeg, W. Malalasekera, *An Introduction to Computational Fluid Dynamics: the Finite Volume Method*, second ed., Pearson Education Ltd., Harlow, England; New York, 2007.
- [32] C.-H. Bruneau, C. Jouron, An efficient scheme for solving steady incompressible Navier-Stokes equations, *J. Comput. Phys.* 89 (1990) 389–413.
- [33] M.M. Gupta, High accuracy solutions of incompressible Navier-Stokes equations, *J. Comput. Phys.* 93 (1991) 343–359.
- [34] H.L. Stone, Iterative solution of implicit approximations of multidimensional partial differential equations, *SIAM J. Numer. Anal.* 5 (1968) 530–558.
- [35] J.S. Reeve, A. Scurr, J.H. Merlin, Parallel versions of Stone's strongly implicit algorithm, *Concurr. Comput.: Pract. Exp.* 13 (2001) 1049–1062.
- [36] M. Wolfe, Loops skewing: the wavefront method revisited, *Int. J. Parallel Prog.* 15 (1986) 279–293.
- [37] L. Dagum, R. Menon, OpenMP: an industry standard API for shared-memory programming, *Comput. Sci. Eng. IEEE* 5 (1998) 46–55.
- [38] J. Cheng, M. Grossman, T. McKercher, *Professional CUDA C Programming*, John Wiley & Sons, 2014.
- [39] Y.-F. Peng, Y.-H. Shiau, R.R. Hwang, Transition in a 2-D lid-driven cavity flow, *Comput. Fluids* 32 (2003) 337–352.
- [40] V. Boppa, J. Gajjar, Global flow instability in a lid-driven cavity, *Int. J. Numer. Meth. Fluids* 62 (2010) 827–853.
- [41] J. Koseff, R. Street, The lid-driven cavity flow: a synthesis of qualitative and quantitative observations, *J. Fluids Eng.* 106 (1984) 390–398.
- [42] J.R. Koseff, R. Street, On end wall effects in a lid-driven cavity flow, *J. Fluids Eng.* 106 (1984) 385–389.
- [43] J. Koseff, R. Street, Visualization studies of a shear driven three-dimensional recirculating flow, *J. Fluids Eng.* 106 (1984) 21–27.
- [44] A.K. Prasad, J.R. Koseff, Reynolds number and end-wall effects on a lid-driven cavity flow, *Phys. Fluids A* 1989–1993 (1) (1989) 208–218.